

# Strain Modulated Superlattices in Graphene

**Authors:** R. Banerjee<sup>1</sup>, V.-H. Nguyen<sup>2</sup>, T. Granzier-Nakajima<sup>1</sup>, L. Pabbi<sup>1</sup>, A. Lherbier<sup>2</sup>, A.R. Binion<sup>1</sup>, J.-C. Charlier<sup>2</sup>, M. Terrones<sup>1</sup>, E.W. Hudson<sup>1\*</sup>

## Affiliations:

<sup>1</sup>Department of Physics, The Pennsylvania State University, University Park, PA 16802, USA

<sup>2</sup>Institute of Condensed Matter and Nanosciences, Université catholique de Louvain, Chemin des étoiles 8, B-1348 Louvain-la-Neuve, Belgium

\*Correspondence to: ehudson@psu.edu

## Abstract:

The quest to create material systems with novel electronic states has led in many cases to the investigation of interfaces. The potential of merging different 2D materials via vertical or horizontal stacking to create van der Waals or lateral heterostructures seems limitless. Here we demonstrate an alternative approach to create 2D heterostructure superlattices. By periodically modulating extreme ( $>10\%$ ) strain in graphene sheets we effectively convert a continuous graphene sheet into a periodic array of lateral heterojunctions. Periodic strain modulation is achieved by draping the graphene sheet over copper step edges and forming nanoscale ripples analogous to those formed in a sheet of fabric pulled taut at its edges. This nanoscale strain modulation creates a periodic array of shorter C-C bond (dense) and longer C-C bond (rare) regions that essentially behave like two different materials. Akin to traditional superlattices, where novel electronic states are created at the interfaces, we find electronic states corresponding to intense interfacial pseudo-gauge fields on the order of 100 T and  $10^7$  V/m. We study these states by scanning tunneling microscopy, spectroscopy and atomistic first principle and model Hamiltonian calculations.

Due to its high electronic mobility, optical transparency, mechanical strength and flexibility, graphene is attractive for electronic applications (1, 2). In this context, different techniques for the manipulation of its electronic properties have been the focus of intense research for the past decade. For example, introducing dopants to the graphene lattice can alter local electronic properties (3–5), while stacking with other 2D materials, either vertically to create Van der Waals heterostructures or in-plane to create lateral heterostructures, can lead to the emergence of novel interfacial states (6–10). In the past several years, graphene superlattices have been found to host exotic electronic states like unconventional superconductivity (11), and non-trivial topological states (12), shown signatures of Hofstadter butterflies (13–16) and demonstrated electronic properties which can be modulated by dynamically twisting layers with respect to one another (17).

Graphene has also been shown to sustain a much larger mechanical deformation (18, 19) than conventional semiconductors, making it an ideal candidate for strain engineering. The application of stress can be efficiently utilized to modulate graphene's electronic properties through the generation of pseudo-gauge fields (20–23). Previous studies of strained graphene have reported the emergence of these pseudo-gauge fields in non-uniform structures like nanobubbles (24) and wrinkles (25–27). In contrast, here we produce and investigate a more regular strain profile in a graphene sheet, making it more amenable for thorough theoretical and experimental explorations.

To engineer such a system, we use low pressure chemical vapor deposition (LPCVD) to grow graphene on electropolished Cu foils at 1020°C (See Supplementary Sec. 1). Previous studies (28) revealed that such high temperatures result in the formation of large Cu steps separated by relatively flat terraces (Fig. 1a). Interestingly, we find that graphene sheets grown by this method form continuous films that are pinned on the flat terraces and drape over the large (up to ~35 nm high) step edges. Upon cooling the sample slowly to 77K, the draped graphene experiences tensile and shear stresses as it gets pulled by the contact forces of the terraces. This leads to periodic arrays of ripples- as imaged by STM (Fig. 1a and c) and qualitatively rendered in Fig. 1b.

To investigate the electronic properties of these strain enabled modulated superlattices (STREMS) we take differential conductance spectra, representative of the local electronic density of states (LDOS), away from and on top of the ripples (at points A and B in Fig. 1c respectively). As shown in Fig. 2a, while spectra taken on the terraces (black curve) display the familiar V-shaped Dirac cone (29), those taken on STREMS (blue curve) reveal a series of peaks. Treating the terrace spectrum as a background, we subtract to determine the strain-induced spectral modification (red curve). The fact that the strain-induced peaks are confined to the STREMS may

be seen in a line-cut (series of spectra) across it (along the red arrow profile of Fig. 1c). We plot twenty seven background-subtracted spectra taken climbing the step edge, along with the height at which they were obtained (Fig. 2c and b respectively), to find that the LDOS peaks appear only in those from the draped and rippled region (#8-19). Interestingly, these peaks are equally spaced in energy, scaling as  $E_n \propto n$  (Fig. 2d). In addition to this energy dependence of the peaks, we also find a spatially-periodic modulation of their amplitude, as shown in a line-cut along the STREMS (Fig. 1c, blue arrow). In Fig. 3a we show that the amplitude of the LDOS peaks (red curve) is closely tied to the z-height profile (black curve), peaking at the ripple crests and troughs.

We first note that these LDOS peaks, we first note that they are remarkably similar to those found in a variety of previous STM measurements of non-flat (e.g. wrinkled or bubbled) graphene (24, 26, 30, 31), and associated with Landau levels arising from strain-induced uniform pseudomagnetic fields. . However, unlike our observed linear scaling, the energies of those peaks were reported to scale as  $E_n \propto \sqrt{n}$ . To clarify the origin of these LDOS peaks and their properties, atomistic calculations based on a  $p_z$  tight-binding Hamiltonian were performed. In particular, a simple model with only the first nearest neighbor couplings was employed (2),  $H_{tb} = \sum_{\langle n,m \rangle} t_{nm} c_n^\dagger c_m$  where the hopping energies  $t_{nm}$  are determined as a function of the C-C bond length  $r_{nm}$  (32):

$$t_{nm} = t_0 \exp \left[ -\beta \left( \frac{r_{nm}}{r_0} - 1 \right) \right] \quad (1)$$

with  $t_0 = -2.6$  eV and  $r_0 = 1.42$  Å. The decay rate  $\beta$  was adjusted to 4.5 by fitting first-principles calculations, while a decay rate value of 3.37 is usually used in flat graphene systems with in-plane deformations only (32). See Supplementary sec. 3 for more details about the calculations.

To mimic the mechanical deformations of the atomically thin sheet, a simple strain profile with out-of-plane displacement fields  $h(y) = h_0 \sin \left( 2\pi \frac{y}{\lambda} \right)$ , with  $\lambda$  being the ripple wavelength, is used to form periodic ripples along the y axis (Fig.3b). In addition, curvature in the draped zone also results in in-plane displacements, which can be modeled by  $u(y) = u_0 \sin \left( 4\pi \frac{y}{\lambda} \right)$ . Although these simple models do not exactly reproduce the triangular ripples observed experimentally, varying these two displacement fields allows us to investigate various deformation situations and hence to clarify the effect of strain fields on the electronic properties of rippled graphene. Indeed, for a given displacement profile  $h(y) + u(y)$ , when  $u_0$  is sufficiently small (or zero), a strain profile is obtained with small C-C bond lengths at the ripple crests and troughs, and larger C-C bond lengths in the regions in between, while for larger  $u_0$ , the opposite situation may occur.

The simulated results obtained in the two situations discussed above (without and with in-plane displacement) are presented in Figs. 3c and 3d, respectively. While both models yield LDOS peaks, the spatial dependence of the amplitudes of those peaks is model dependent. In the first, higher amplitude peaks occur at the middle of the ripples (Fig. 3c), while in the second they occur at the crests and troughs (Fig. 3d). The latter is consistent with our measurements (Fig. 3a). Thus in-plane displacement must to be included ( $u(y) \neq 0$ ) implying that both displacement fields

$h(y) + u(y)$  concurrently occur and play a major role in the electronic properties of rippled graphene. Finally, the LDOS is characterized by a series of almost equidistant peaks with a peak spacing  $\sim 80$  meV, consistent with the experimentally observed 69(3) meV.

It has been shown that the effects of any strain field in graphene can be modeled by pseudo-magnetic and electric fields (20, 30, 33), with the corresponding pseudo-vector  $\vec{A}$  and scalar  $V_S$  potentials can be determined in the continuous approximation as a function of the strain tensor  $u_{ij}(\vec{r})$  (22, 34, 35):

$$A_x - iA_y = \pm \frac{\hbar\beta}{2er_0} (u_{xx} - u_{yy} + 2iu_{xy}) \quad (2)$$

$$V_S = \frac{\epsilon'_0 r_0}{2} (u_{xx} + u_{yy}) \quad (3)$$

where  $u_{ij} \equiv \frac{1}{2} \left( \frac{\partial u_i}{\partial r_j} + \frac{\partial u_j}{\partial r_i} \right) + \frac{1}{2} \frac{\partial h}{\partial r_i} \frac{\partial h}{\partial r_j}$ . The  $\pm$  signs in Eq. (2) correspond to the vector potential applied to fermions in the  $K/K'$  valleys of the graphene Brillouin zone, respectively.

In STREMS, the periodic nature of the displacement profile and hence  $u_{ij}$  implies the existence of spatially periodic pseudo magnetic and electric fields. To check that this accurately describes the electronic properties of our system, we not only use the strained tight-binding model described above, but also create an effective model of unstrained flat graphene with a tight binding Hamiltonian, pseudomagnetic field  $\vec{B}_S = B_{max} \sin\left(4\pi \frac{y}{\lambda}\right) \vec{e}_z$  and potential energy  $V_S = V_{max} \cos\left(4\pi \frac{y}{\lambda}\right)$ . LDOS maps from these two models are displayed in Fig. 4a and b respectively. The result obtained by an unstrained model (Fig. 4b) including the combination effects of spatially varying (E, B) fields is in good agreement with that obtained in the periodically strained system discussed above and presented in Fig. 4a. This implies that both pseudo magnetic and electric fields are induced by the corresponding strain field. For a more detailed explanation for the requirement of pseudo electric fields in addition to pseudo magnetic fields, and to explain the spatial variation of the observed spectra, see Supplementary sec. 4.

With this information we now have a complete picture of the STREMS, rendered qualitatively in Fig. 5. A spatially varying strain profile modulates the C-C bonds in graphene, effectively creating a superlattice of regions which are locally dense (purple) and rare (gold) (Fig. 5a). Pseudopotentials arise from this strain, and their associated pseudo-fields (Fig. 5b), which are spatial derivatives of the potentials, become large in the presence of strain gradients – which are maximized at the interface between dense and rare regions. This is analogous to traditional superlattices, where novel electronic states arise at the interfaces. For rippled graphene, these interfacial states are describable by pseudo B and E fields. From tight-binding calculations, we find that pseudo-magnetic fields of 100T are required to match the experimental data. Such intense fields are created by extreme strain magnitudes, measuring over 10%, as estimated by first-

principles calculations (Supplementary sec. 3) and measured by imaging the graphene lattice directly (Supplementary sec. 5).

Note that the observation of equally spaced peaks in the LDOS corresponds to a quasi-quantization  $E_n \propto n$ , in contrast to the well-known  $E_n \propto \sqrt{n}$  scaling observed when Landau levels arise from spatially uniform magnetic fields in graphene (24, 26, 30, 31, 36). This linearity is an effect of having spatially periodic pseudo-magnetic fields(37). In particular, as rendered in Fig. 5b, alternating zones of oppositely directed pseudo-magnetic fields should lead to the formation of valley polarized edge states (22, 37–39). Interaction between these edge states essentially alters the observed quantization picture compared to uniform field situation. These edge states can have snake-like trajectories (40) due to the valley dependent pseudomagnetic field directions (41–43), and are a potential candidate for studying valley-transport phenomena.

In addition to the observed phenomena, many other theoretical proposals, including valley filters and electron optics in graphene require localized magnetic barriers (44–52). Such longstanding proposals have largely remained experimentally unrealized as they require magnetic field profiles that are simultaneously sufficiently strong and inhomogeneous at a length scale smaller than the electronic mean free path. Though the laws of electromagnetism do not forbid the existence of such fields, they are difficult to generate in practice as strong magnetic fields created by large magnets are homogeneous at the length scale of most samples, while only weak inhomogeneous fields can be applied, for example by local magnetic strips. With our realization of pseudo-fields which are simultaneously intense ( $\sim 100$  T) and modulated on short length scales ( $\sim$ few nm), we can finally begin to realize these proposals not only in graphene but in a wide variety of 2D materials which should also support STREMS and where strain is known to significantly influence electronic properties (23, 53–56). The intensity of these inhomogeneous pseudo-fields should make realization of these proposals possible even at room temperatures (24).

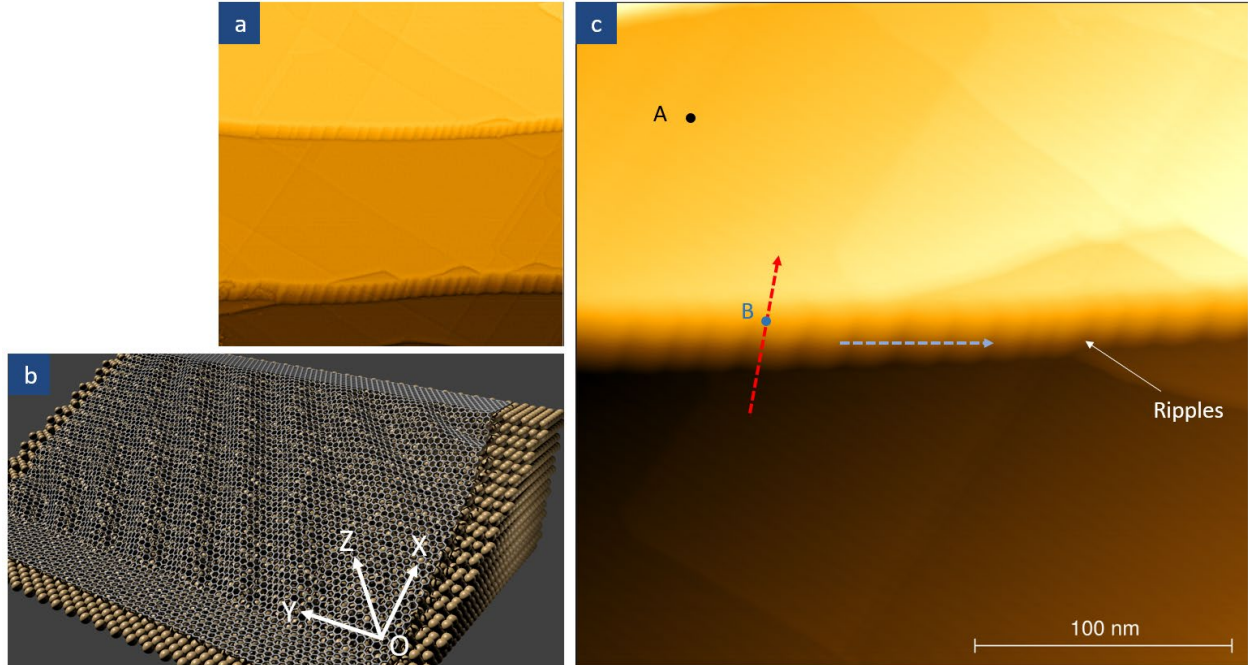


**Figure 1. STREMS topography and model.** (a) STM topography of 450 nm square region shows graphene draped over two steps, each about 20 nm high, leading to ripples (current setpoint  $I_{\text{set}} = 62$  pA, sample bias  $V_s = 0.1$  V). (b) Artistic rendition identifying the coordinate system used throughout this work. (c) STM topography zooming in on a step edge, highlighting locations at which data presented in later figures was obtained.  $I_{\text{set}} = 80$  pA,  $V_s = 0.1$  V. All topographic data is obtained at  $T = 80$  K and unfiltered.

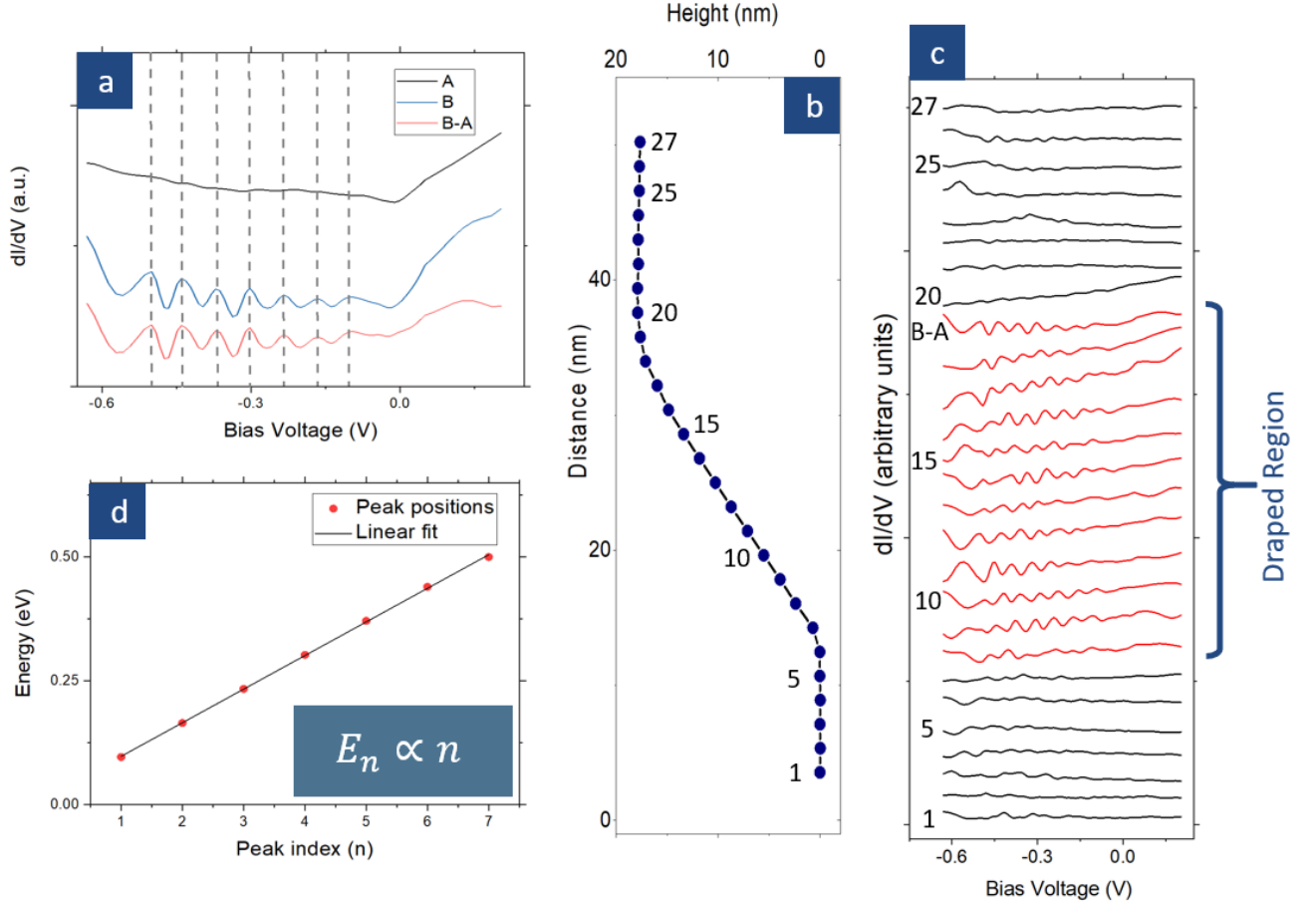


**Figure 2. Spectroscopy across a STREMS.** (a) Differential conductance spectra taken (A) away from and (B) on a STREMS (locations in Fig. 1c). Spectrum (A) has the Dirac point near the Fermi energy ( $V = 0$  V). Treating (A) as background, subtraction highlights a series of peaks in the LDOS. (b) A line cut rising across the STREMS (along red arrow of Fig. 1c) shows that peaks in the background subtracted spectra (c) only appear in the draped region (labelled #8-19, colored red). All these peaks are equally spaced, as shown in (d), plotted for the peaks in spectrum shown in (a), with slope = 67.83(5) meV/peak. For the twelve such spectra in (c), the average slope of energy vs. index plots is 69(3) meV/peak. See Supplementary sec. 6 for linear fits to all spectra taken on the draped region. All spectra are obtained using standard lock-in techniques, with 13mV bias modulation at  $\sim 971$  Hz.

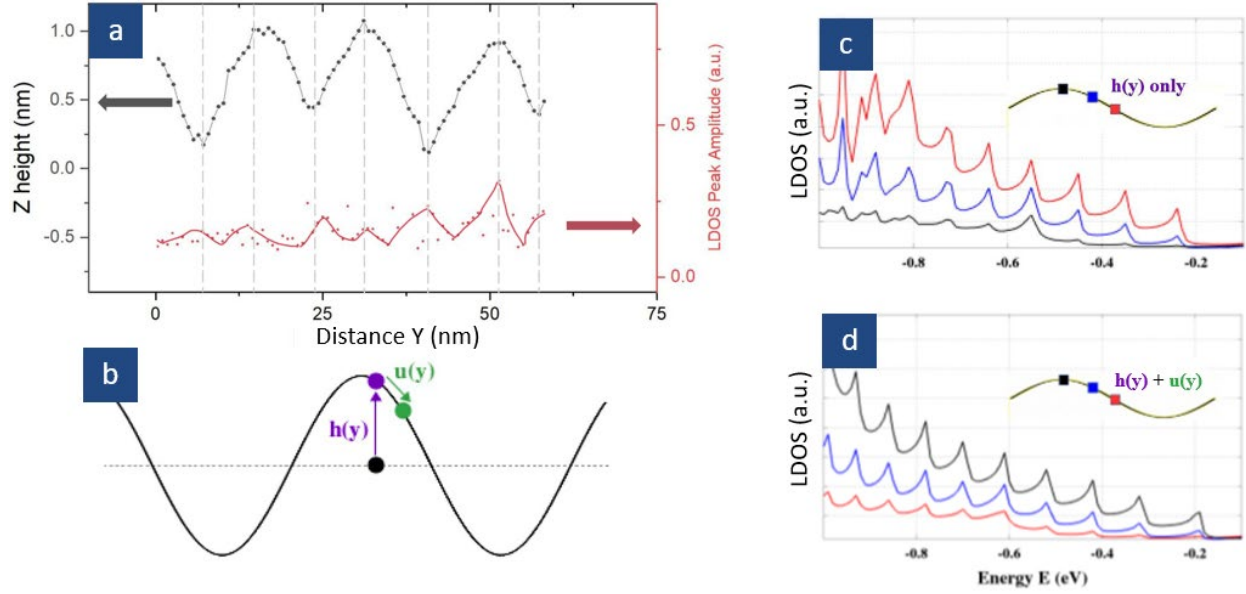


**Figure 3. Peak amplitude along the ripple.** (a) A line cut along the ripple (blue arrow in Fig. 1c) reveals that the amplitude of LDOS peaks (red) is maximized at the crests and troughs of the nearly triangular ripples (black). All lines are guides to the eye. (b) Displacement (out-of-plane  $h(y)$  and in-plane  $u(y)$ ) fields to be considered in rippled graphene. Simulated LDOS as a function of electron energy obtained when only out-of-plane displacements are considered (c) and when in-plane displacements are added (d) show that in-plane displacements are necessary to match the experimental results. Simulations calculated using displacement parameters  $\lambda = 20$  nm,  $h_0 = 2.5$  nm and  $u_0 = 3.5$  Å.



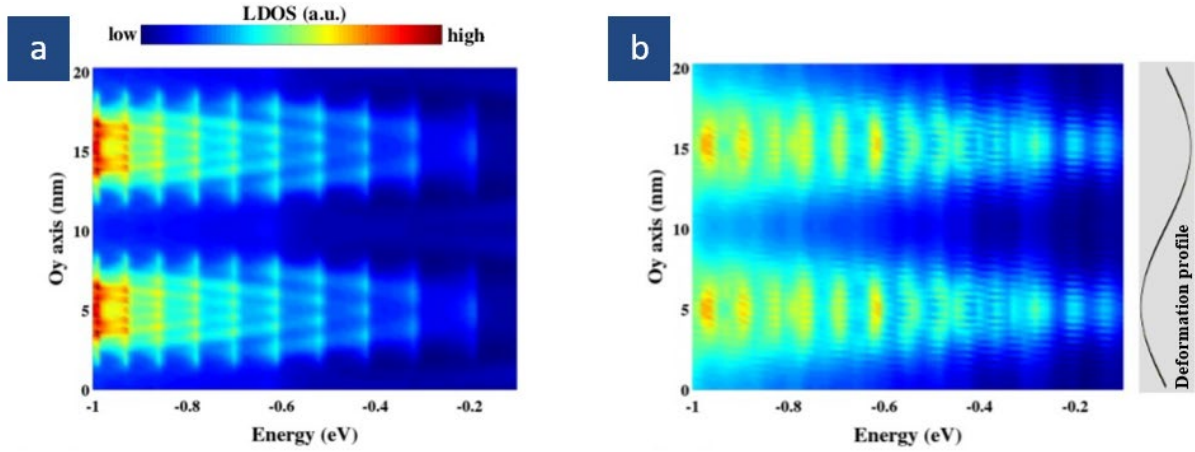


**Figure 4. LDOS spatial/energy maps.** LDOS spatial/energy maps. Both (a) Strained and (b) unstrained + pseudopotential tight binding models capture important features in spectroscopy obtained along the ripple (blue arrow in Fig. 1c). The LDOS amplitudes are higher at the crests and troughs of the ripples, as observed experimentally (Fig. 3a). The simulation also captures the feature of having higher LDOS weight at large negative biases, as observed in Fig. 2a.

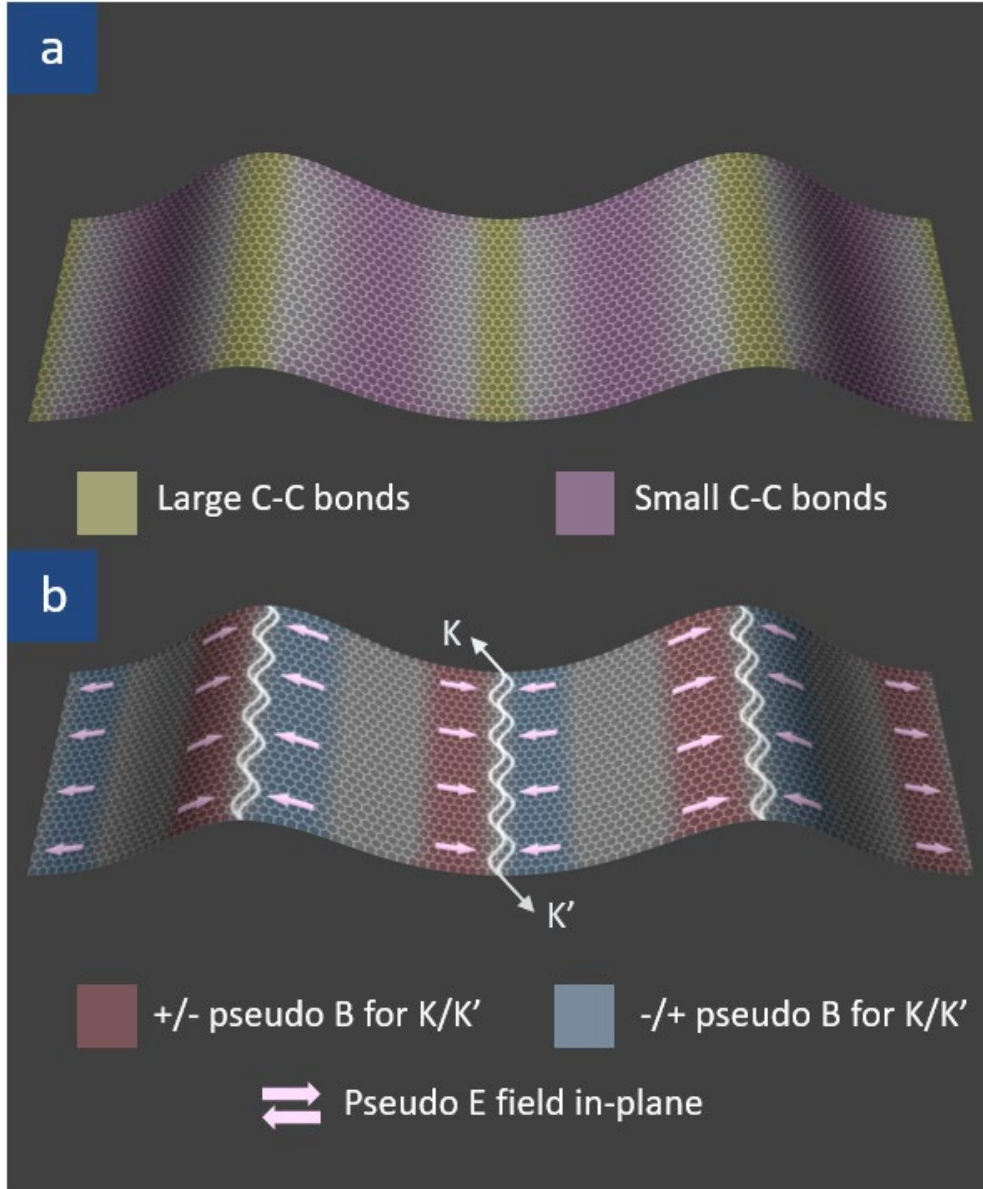


**Figure 5. Artistic rendition of STREMS.** (a) The strain associated with rippling creates rare (gold) and dense (purple) regions in the graphene, effectively acting as two different materials in a superlattice. (b) Pseudo-fields form near the interfaces of these “materials,” both electric (pink arrows) and magnetic (red/blue regions indicating the  $\pm\hat{z}$  field direction for pseudospin up electrons). LDOS peaks are maximized at the ripple crests and troughs, where valley polarized snake states (white curved lines) are also expected to form due to the reversal of the pseudospin dependent pseudo-magnetic fields across these lines.

## References and Notes:

1. A. K. Geim, K. S. Novoselov, The rise of graphene | Nature Materials. *Nature Materials*. **6**, 183–191 (2007).
2. A. H. Castro Neto, F. Guinea, N. M. R. Peres, K. S. Novoselov, A. K. Geim, The electronic properties of graphene. *Reviews of Modern Physics*. **81**, 109–162 (2009).
3. H. Liu, Y. Liu, D. Zhu, Chemical doping of graphene. *J. Mater. Chem.* **21**, 3335–3345 (2011).
4. R. Lv *et al.*, Nitrogen-doped graphene: beyond single substitution and enhanced molecular sensing. *Scientific Reports*. **2**, 586 (2012).
5. L. Zhao *et al.*, Visualizing Individual Nitrogen Dopants in Monolayer Graphene. *Science*. **333**, 999–1003 (2011).
6. A. K. Geim, I. V. Grigorieva, Van der Waals heterostructures. *Nature*. **499**, 419–425 (2013).
7. K. S. Novoselov, A. Mishchenko, A. Carvalho, A. H. Castro Neto, 2D materials and van der Waals heterostructures. *Science*. **353**, aac9439 (2016).
8. X. Ling *et al.*, Parallel Stitching of 2D Materials. *Advanced Materials*. **28**, 2322–2329 (2016).
9. M. P. Levendorf *et al.*, Graphene and boron nitride lateral heterostructures for atomically thin circuitry. *Nature*. **488**, 627–632 (2012).
10. X. Duan *et al.*, Lateral epitaxial growth of two-dimensional layered semiconductor heterojunctions. *Nature Nanotechnology*. **9**, 1024–1030 (2014).
11. Y. Cao *et al.*, Unconventional superconductivity in magic-angle graphene superlattices. *Nature*. **556**, 43–50 (2018).
12. R. V. Gorbachev *et al.*, Detecting topological currents in graphene superlattices. *Science*. **346**, 448–451 (2014).
13. C. R. Dean *et al.*, Hofstadter’s butterfly and the fractal quantum Hall effect in moiré superlattices. *Nature; London*. **497**, 598–602 (2013).
14. B. Hunt *et al.*, Massive Dirac Fermions and Hofstadter Butterfly in a van der Waals Heterostructure. *Science*. **340**, 1427–1430 (2013).
15. R. K. Kumar *et al.*, High-order fractal states in graphene superlattices. *PNAS*. **115**, 5135–5139 (2018).
16. L. A. Ponomarenko *et al.*, Cloning of Dirac fermions in graphene superlattices. *Nature*. **497**, 594–597 (2013).

17. R. Ribeiro-Palau *et al.*, Twistable electronics with dynamically rotatable heterostructures. *Science*. **361**, 690–693 (2018).
18. C. Lee, X. Wei, J. W. Kysar, J. Hone, Measurement of the Elastic Properties and Intrinsic Strength of Monolayer Graphene. *Science*. **321**, 385–388 (2008).
19. R. Roldán, A. Castellanos-Gomez, E. Cappelluti, F. Guinea, Strain engineering in semiconducting two-dimensional crystals. *J. Phys.: Condens. Matter*. **27**, 313201 (2015).
20. F. Guinea, B. Horovitz, P. Le Doussal, Gauge field induced by ripples in graphene. *Phys. Rev. B*. **77**, 205421 (2008).
21. F. Guinea, M. I. Katsnelson, M. A. H. Vozmediano, Midgap states and charge inhomogeneities in corrugated graphene. *Phys. Rev. B*. **77**, 075422 (2008).
22. F. Guinea, M. I. Katsnelson, A. K. Geim, Energy gaps and a zero-field quantum Hall effect in graphene by strain engineering. *Nature Physics*. **6**, 30–33 (2010).
23. G. G. Naumis, S. Barraza-Lopez, M. Oliva-Leyva, H. Terrones, Electronic and optical properties of strained graphene and other strained 2D materials: a review. *Rep. Prog. Phys.* **80**, 096501 (2017).
24. N. Levy *et al.*, Strain-Induced Pseudo-Magnetic Fields Greater Than 300 Tesla in Graphene Nanobubbles. *Science*. **329**, 544–547 (2010).
25. L. Tapasztó *et al.*, Breakdown of continuum mechanics for nanometre-wavelength rippling of graphene. *Nature Physics*. **8**, 739–742 (2012).
26. L. Meng *et al.*, Strain-induced one-dimensional Landau level quantization in corrugated graphene. *Phys. Rev. B*. **87**, 205405 (2013).
27. M. L. Teague *et al.*, Evidence for Strain-Induced Local Conductance Modulations in Single-Layer Graphene on SiO<sub>2</sub>. *Nano Lett.* **9**, 2542–2546 (2009).
28. D. Yi *et al.*, What Drives Metal-Surface Step Bunching in Graphene Chemical Vapor Deposition? *Phys. Rev. Lett.* **120**, 246101 (2018).
29. G. M. Rutter *et al.*, Scattering and Interference in Epitaxial Graphene. *Science*. **317**, 219–222 (2007).
30. Y. Liu *et al.*, Tailoring sample-wide pseudo-magnetic fields on a graphene–black phosphorus heterostructure. *Nature Nanotechnology*. **13**, 828 (2018).
31. Y. Jiang *et al.*, Visualizing Strain-Induced Pseudomagnetic Fields in Graphene through an hBN Magnifying Glass. *Nano Lett.* **17**, 2839–2843 (2017).
32. V. M. Pereira, A. H. Castro Neto, N. M. R. Peres, Tight-binding approach to uniaxial strain in graphene. *Phys. Rev. B*. **80**, 045401 (2009).

33. Z. Qi *et al.*, Pseudomagnetic fields in graphene nanobubbles of constrained geometry: A molecular dynamics study. *Phys. Rev. B.* **90**, 125419 (2014).
34. H. Suzuura, T. Ando, Phonons and electron-phonon scattering in carbon nanotubes. *Physical Review B.* **65** (2002), doi:10.1103/PhysRevB.65.235412.
35. H. Shioya, S. Russo, M. Yamamoto, M. F. Craciun, S. Tarucha, Electron States of Uniaxially Strained Graphene. *Nano Letters.* **15**, 7943–7948 (2015).
36. S.-Y. Li *et al.*, Observation of unconventional splitting of Landau levels in strained graphene. *Phys. Rev. B.* **92**, 245302 (2015).
37. M. R. Masir, P. Vasilopoulos, F. M. Peeters, Magnetic Kronig–Penney model for Dirac electrons in single-layer graphene. *New J. Phys.* **11**, 095009 (2009).
38. V. H. Nguyen, J.-C. Charlier, Stepped Graphene-based Aharonov-Bohm Interferometers. *arXiv:1812.02845 [cond-mat]* (2018) (available at <http://arxiv.org/abs/1812.02845>).
39. A. Kormányos, P. Rakya, L. Oroszlány, J. Cserti, Bound states in inhomogeneous magnetic field in graphene: Semiclassical approach. *Physical Review B.* **78** (2008), doi:10.1103/PhysRevB.78.045430.
40. F. Evers, A. D. Mirlin, D. G. Polyakov, P. Wölfle, Semiclassical theory of transport in a random magnetic field. *Phys. Rev. B.* **60**, 8951–8969 (1999).
41. M. Settnes, S. R. Power, M. Brandbyge, A.-P. Jauho, Graphene Nanobubbles as Valley Filters and Beam Splitters. *Phys. Rev. Lett.* **117**, 276801 (2016).
42. T. K. Ghosh, A. De Martino, W. Häusler, L. Dell’Anna, R. Egger, Conductance quantization and snake states in graphene magnetic waveguides. *Phys. Rev. B.* **77**, 081404 (2008).
43. L. Oroszlány, P. Rakya, A. Kormányos, C. J. Lambert, J. Cserti, Theory of snake states in graphene. *Physical Review B.* **77** (2008), doi:10.1103/PhysRevB.77.081403.
44. M. Ramezani Masir, P. Vasilopoulos, A. Matulis, F. M. Peeters, Direction-dependent tunneling through nanostructured magnetic barriers in graphene. *Physical Review B.* **77** (2008), doi:10.1103/PhysRevB.77.235443.
45. M. Ramezani Masir, P. Vasilopoulos, F. M. Peeters, Fabry-Pérot resonances in graphene microstructures: Influence of a magnetic field. *Physical Review B.* **82** (2010), doi:10.1103/PhysRevB.82.115417.
46. M. R. Masir, P. Vasilopoulos, F. M. Peeters, Kronig–Penney model of scalar and vector potentials in graphene. *J. Phys.: Condens. Matter.* **22**, 465302 (2010).
47. M. R. Masir, P. Vasilopoulos, F. M. Peeters, Graphene in inhomogeneous magnetic fields: bound, quasi-bound and scattering states. *J. Phys.: Condens. Matter.* **23**, 315301 (2011).

48. L. Z. Tan, C.-H. Park, S. G. Louie, Graphene Dirac fermions in one-dimensional inhomogeneous field profiles: Transforming magnetic to electric field. *Physical Review B*. **81** (2010), doi:10.1103/PhysRevB.81.195426.
49. L. Dell'Anna, A. De Martino, Multiple magnetic barriers in graphene. *Physical Review B*. **79** (2009), doi:10.1103/PhysRevB.79.045420.
50. S. Ghosh, M. Sharma, Electron optics with magnetic vector potential barriers in graphene. *J. Phys.: Condens. Matter*. **21**, 292204 (2009).
51. A. De Martino, L. Dell'Anna, R. Egger, Magnetic Confinement of Massless Dirac Fermions in Graphene. *Phys. Rev. Lett.* **98**, 066802 (2007).
52. Z. Wu, F. Zhai, F. M. Peeters, H. Q. Xu, K. Chang, Valley-Dependent Brewster Angles and Goos-Hänchen Effect in Strained Graphene. *Physical Review Letters*. **106** (2011), doi:10.1103/PhysRevLett.106.176802.
53. Y. Okada *et al.*, Visualizing Landau Levels of Dirac Electrons in a One-Dimensional Potential. *Phys. Rev. Lett.* **109**, 166407 (2012).
54. I. Zeljkovic *et al.*, Strain engineering Dirac surface states in heteroepitaxial topological crystalline insulator thin films. *Nature Nanotechnology*. **10**, 849–853 (2015).
55. W. Wei, Y. Dai, B. Huang, Straintronics in two-dimensional in-plane heterostructures of transition-metal dichalcogenides. *Phys. Chem. Chem. Phys.* **19**, 663–672 (2016).
56. D. Akinwande *et al.*, A review on mechanics and mechanical properties of 2D materials—Graphene and beyond. *Extreme Mechanics Letters*. **13**, 42–77 (2017).
57. D. Nečas, P. Klapetek, Gwyddion: an open-source software for SPM data analysis. *centr.eur.j.phys.* **10**, 181–188 (2012).
58. A. Das *et al.*, Monitoring dopants by Raman scattering in an electrochemically top-gated graphene transistor. *Nature Nanotechnology*. **3**, 210–215 (2008).
59. A. C. Ferrari *et al.*, Raman Spectrum of Graphene and Graphene Layers. *Phys. Rev. Lett.* **97**, 187401 (2006).
60. R. Carrillo-Bastos, D. Faria, A. Latgé, F. Mireles, N. Sandler, Gaussian deformations in graphene ribbons: Flowers and confinement. *Phys. Rev. B*. **90**, 041411 (2014).
61. Y. Wu *et al.*, Quantum Wires and Waveguides Formed in Graphene by Strain. *Nano Lett.* **18**, 64–69 (2018).
62. J. Lee *et al.*, Imaging electrostatically confined Dirac fermions in graphene quantum dots. *Nature Physics*. **12**, 1032–1036 (2016).

63. Y. Jiang *et al.*, Tuning a circular p–n junction in graphene from quantum confinement to optical guiding. *Nature Nanotechnology*. **12**, 1045–1049 (2017).
64. V. M. Pereira, A. H. Castro Neto, Strain Engineering of Graphene’s Electronic Structure. *Phys. Rev. Lett.* **103**, 046801 (2009).
65. M. Gibertini, A. Tomadin, M. Polini, A. Fasolino, M. I. Katsnelson, Electron density distribution and screening in rippled graphene sheets. *Phys. Rev. B*. **81**, 125437 (2010).
66. V. M. Pereira, A. H. Castro Neto, H. Y. Liang, L. Mahadevan, Geometry, Mechanics, and Electronics of Singular Structures and Wrinkles in Graphene. *Phys. Rev. Lett.* **105**, 156603 (2010).
67. G. W. Jones, D. A. Bahamon, A. H. Castro Neto, V. M. Pereira, Quantized Transport, Strain-Induced Perfectly Conducting Modes, and Valley Filtering on Shape-Optimized Graphene Corbino Devices. *Nano Lett.* **17**, 5304–5313 (2017).
68. M. Mucha-Kruczyński, V. I. Fal’ko, Pseudo-magnetic field distribution and pseudo-Landau levels in suspended graphene flakes. *Solid State Communications*. **152**, 1442–1445 (2012).
69. N. N. Klimov *et al.*, Electromechanical Properties of Graphene Drumheads. *Science*. **336**, 1557–1561 (2012).

**Acknowledgments:** We thank V. Crespi, J.A. Strosio, P.N. First, H.J. Hug and J.K. Jain for helpful discussions.

**Funding:** This material is based upon work supported by the National Science Foundation under Grant No. 1229138. T.G.N and M.T. acknowledge The Air Force Office of Scientific Research (AFOSR) grant 17RT0244. V.-H.N, A.L. and J.-C.C. acknowledge financial support from the the Francqui foundation and the F.R.S.-FNRS of Belgium through the research project (T.1077.15), from the Flag-Era JTC 2017 project “MECHANIC” (R.50.07.18.F), from the Fédération Wallonie-Bruxelles through the ARC on 3D nanoarchitecturing of 2D crystals (16/21-077), and from the European Union’s Horizon 2020 research and innovation program (696656).

**Author contributions:** R.B. conceived the project; R.B., L.P. built the custom instrument; T.G.N. prepared the samples; R.B., L.P. collected the data; R.B. performed analysis and did observations on the data; V.H.N., A.L. performed theoretical modeling; all authors took part in interpreting the results; R.B., V.H.N., T.G.N., A.L., J.-C.C, M.T., E.W.H. wrote the paper; J.C.C., M.T., E.W.H. advised.

**Competing interests:** Authors declare no competing interests

**Data and materials availability:** All data is available in the main text or the supplementary materials.

## Supplementary Materials:

### Methods:

All data was obtained at 80 K in a custom built ultra-high vacuum (UHV) STM system using a SPECS Tyto head with cut Pt-Ir (80%-20%) tips. Part of the analysis was done using the software Gwyddion (57). Though similar results have been observed with multiple tips on multiple samples, for consistency and calibration, all results presented here are obtained with a single tip on the same sample. Samples were transferred to the UHV environment within 10 minutes of growth to minimize air exposure. The sample was annealed at 300° C for about 1.5 hours in UHV to evaporate any adsorbent that might have settled on the surface during the transfer process. Similar observations have been made even after multiple annealing processes.

### S1. LPCVD growth and Raman characterization of graphene:

Growth was performed in a low-pressure quartz tube furnace. A piece of electropolished copper was placed in a quartz tube and positioned in the center of a high temperature furnace. A boat containing ammonia-borane was placed in the tube upstream of the furnace and wrapped with a heating belt. Subsequently the tube was pumped down to  $10^{-2}$  Torr and flushed with 37.5 sccm  $H_2$  and 212.5 sccm Ar gas for several minutes. Afterwards the gas was left flowing and the furnace temperature is raised to 1020°C at which point the heating belt was set for 50 °C. When the heating belt reaches the set temperature 10 sccm methane was flowed through the furnace for 5 min. Afterwards the methane is shut off and the furnace cooled naturally to room temperature. Some Boron and Nitrogen dopant atoms were seen embedded in the graphene lattice. They show up clearly as bright spots with STM due to their higher density of states. None were seen in regions where the strained graphene was observed. Raman spectroscopy (Fig. S1) shows that the graphene is indeed monolayer with a characteristic 2D peak.

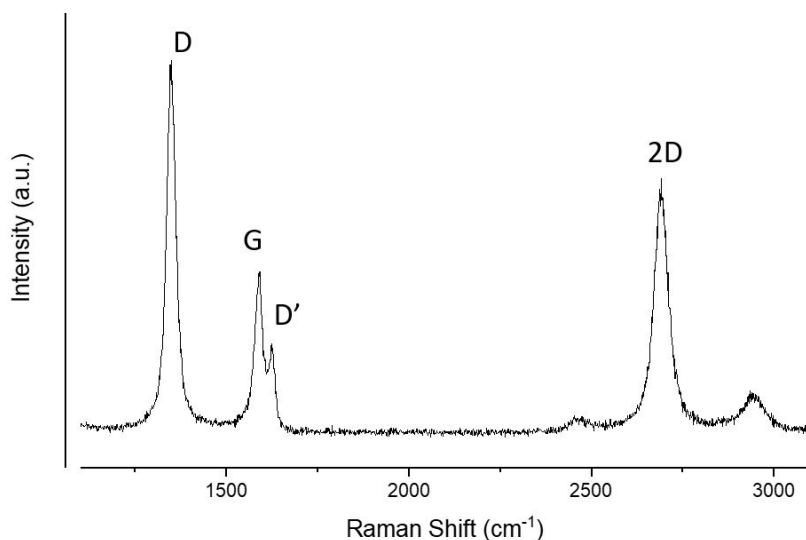




**Figure S1** Raman spectrum shows the 2D nature of the graphene sheet(58, 59).

## **S2: Other possible origins of LDOS peaks**

Electrons in graphene can be confined by strain(60, 61), and so it is important to consider whether the LDOS peaks we observe are effects of electrons trapped in a confining potential due to strain barriers created by ripple crests and troughs. Pseudo-electric barriers due to charge redistributions should be ineffective in confining electrons impinging perpendicularly on them due to Klein tunneling(62). Pseudo-magnetic barriers, if strong enough can confine electrons in such a case(51), and such a hypothesis can be tested directly by taking spectra on regions with different ripple wavelengths. We expect the energy spacing between LDOS peaks to be reduced as the width of the confining potential is increased. In Fig. S2, we plot the spectra taken on two regions with crest-to-trough distance of 11.2 nm (red) and 7.6 nm (black) taken on the same step edge. The energy spacing for both are almost same, in contrast to confinement effects(63).

In general, the energy spacing should be a function of the wavelength  $\lambda$ , maximum out-of-plane displacement  $h_0$  and maximum in-plane stretching  $u_0$ . First principle LDOS calculations performed on rippled graphene show that the dependence on wavelength is indeed very weak (Fig. S2 b, c), as observed. Thus, while a quantization purely due to electrostatic confinement can create states with energy spacing strongly dependent on the width of the barrier(63), strong spatially varying pseudo-magnetic fields markedly modify this quantization.

These peaks also cannot be defect states as the formation of small single atom defects are energetically favorable (4) but we see these peaks over tens of nanometers in either directions. Also, the peak positions remain unchanged for different tip heights – as would be expected if the defect states got charged. Care was also taken to dispel any adsorbed impurities on the surface by annealing the sample in UHV (See Methods section).

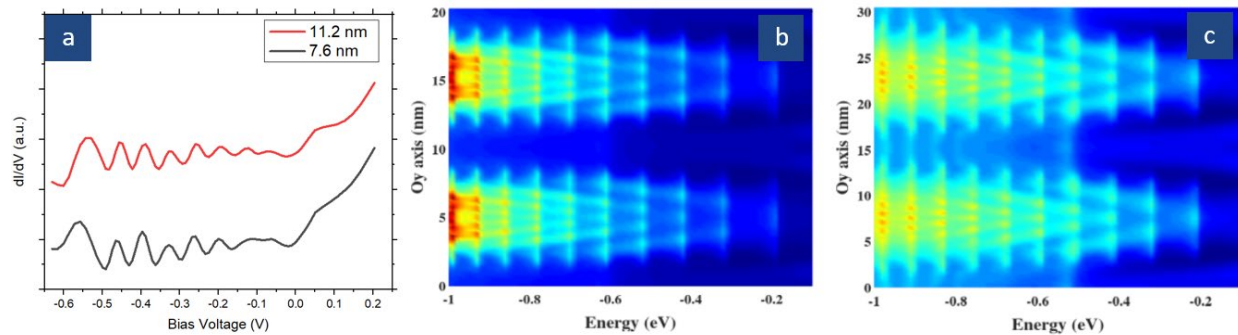


**Figure S2:** (a) Spectra taken on two regions on the same step edge with different ripple crest-to-trough distance show similar peak energies. If these peaks were resulting from a confinement effect caused by strain barriers, then the energy spacing of the levels would vary significantly as the width of the confining potential varied. Legend refers to the crest-to-trough distance of the ripple

edge where the spectra were taken. Spectra obtained with 13 mV bias modulation at  $\sim 971$  Hz. (b and c) First principle calculations concurring with this result. (b) and (c) have ripple wavelengths of 10 nm and 15 nm respectively but show similar LDOS energy spacings.

### S3. Modeling methodologies: Tight binding versus DFT Calculations

Calculations based on tight-binding (TB) Hamiltonians have been demonstrated to be the most efficient approach to investigate the electronic properties of graphene systems, especially when their dimension reaches the nanometer regime. A tight-binding Hamiltonian adjusted due to the lattice deformations (32) is also able to compute accurately the effects of strain and to develop the theoretical models for analyzing the strain-induced pseudo-fields in graphene(20, 33, 41, 64–67). In particular, a first nearest-neighbor  $p_z$ -orbitals model,  $H_{tb} = \sum_{\langle n,m \rangle} t_{nm} c_n^\dagger c_m$ , with exponential dependence of the hopping energy  $t_{nm}$  on the C-C bond length  $r_{nm}$ ,  $t_{nm} = t_0 \exp[-\beta(r_{nm}/r_0 - 1)]$ , has been validated and widely employed to investigate the electronic properties of strained graphene without and even with small curvature(20, 33, 41). In the rippled graphene systems considered here, a significant curvature is, however, obtained. Hence, the validity of the presented tight-binding model was re-examined, by fitting to the first-principles calculations. In particular, Density Functional Theory (DFT) calculations implemented in the SIESTA package were performed to compute the electronic band-structure of reasonably small rippled systems and, accordingly, the hopping parameters of the TB Hamiltonian were properly adjusted to agree with the obtained DFT data.

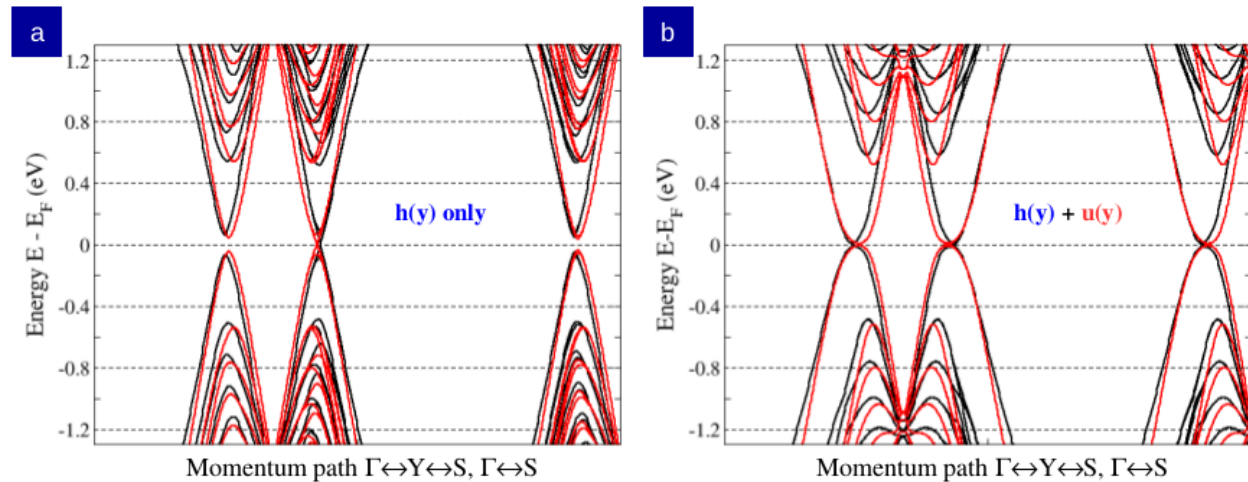


Fig. S3: Band structure of rippled graphene systems (a) without and (b) with in-plane displacements: tight binding approach (red curves) versus DFT calculations (black curves). Ripple parameters  $\lambda = 10$  nm,  $h_0 = 1.0$  nm and  $u_0 = 2.0$  Å are considered.

The band-structures of rippled graphene systems with  $\lambda = 10$  nm,  $h_0 = 1.0$  nm and  $u_0 = 2.0$  Å obtained by both DFT and our adjusted TB calculations are presented in Fig. S3. To get the best fit between these two calculations, the decay rate  $\beta$  of the TB Hamiltonian has to be adjusted to  $\sim 4.5$  while a value of 3.37 is usually used in flat graphene systems with in-plane deformations only (32). The value of  $\beta \approx 4.5$  corresponds to extreme strain magnitudes in graphene ( $>10\%$ ), which is consistent with direct strain measurements shown in Supplementary sec. 5. The validity of this adjusted TB Hamiltonian is further confirmed by the LDOS maps presented in Figs. S4(a, b). This TB Hamiltonian was finally employed to investigate the electronic spectra of rippled graphene systems, presented in the main text, with similar sizes as in the experiments.

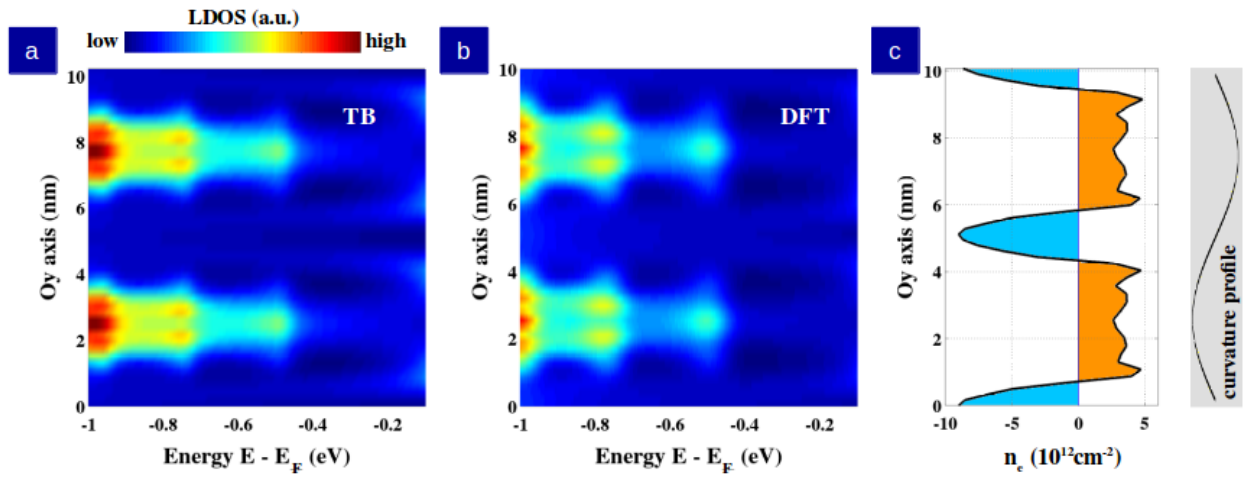


Fig. S4: LDOS maps obtained by tight-binding (a) and DFT calculations (b). (c) Local charge density along the ripple axis obtained by DFT calculations. The rippled graphene system in Fig. S3b is considered here.

In addition, the *ab initio* calculations were also used to compute the local charge density presented in Fig. S4c along the ripple of the system studied in Figs. S3b. It is shown that due to its lattice (hence, electronic) inhomogeneity, the charge carriers are redistributed and hence a non-uniform local charge density is observed along the ripple axis. This result essentially explains the necessity of taking into account both pseudo-magnetic and electric fields in the effective calculations, as presented in the main text, to accurately depict the electronic properties of the system.

#### S4. Observation of pseudo-electric fields

Note that even though both pseudo-magnetic and electric fields can be induced by a strain field, it has been shown that the electric field is generally less pronounced (30, 65, 66, 68), because of screening effects. As discussed in the previous section, a doping inhomogeneity is actually

obtained along the ripple axis, thus implying that the pseudo-electric fields also occur and can play an important role on the electronic properties of the considered rippled systems. This is demonstrated in the main text by comparison between calculations using a strained TB Hamiltonian and an unstrained one with pseudo-fields and is further confirmed by the analysis below.

First, if only the pseudo-magnetic field above occurs, there are two zones of positive fields alternatively with two other zones of negative ones in each periodic unit of rippled graphene. Under the effect of such magnetic fields, opposite edge states are formed inside the zones of opposite fields and accordingly four LDOS peaks (around the interface between these zones) are observed in one periodic unit of rippled graphene, i.e., LDOS is a periodic function along the ripple axis with a periodic length  $\lambda/4$  as illustrated in Fig.S5a. However, this is not the case observed in experiments and confirmed by calculations using the strained tight-binding Hamiltonian, i.e., a periodic length  $\lambda/2$  is obtained. Such a picture can be however obtained when both pseudo-magnetic field and electric fields are considered (Fig. 4b of main text). When a pseudo electric field (i.e., periodic potential energy as considered) is added, the spatial variation of the potential energy gives rise to another feature that redistributes electrons, leading to much more available hole edge states in the local zone of high potential energies whereas the number of hole edge states in the local zone of low potential energies are reduced (see Fig. S4b). The existence of this electric field and accordingly the corresponding charge redistribution (i.e., inhomogeneous distribution of charges) is further confirmed by *DFT* calculations (see Fig. S4c).

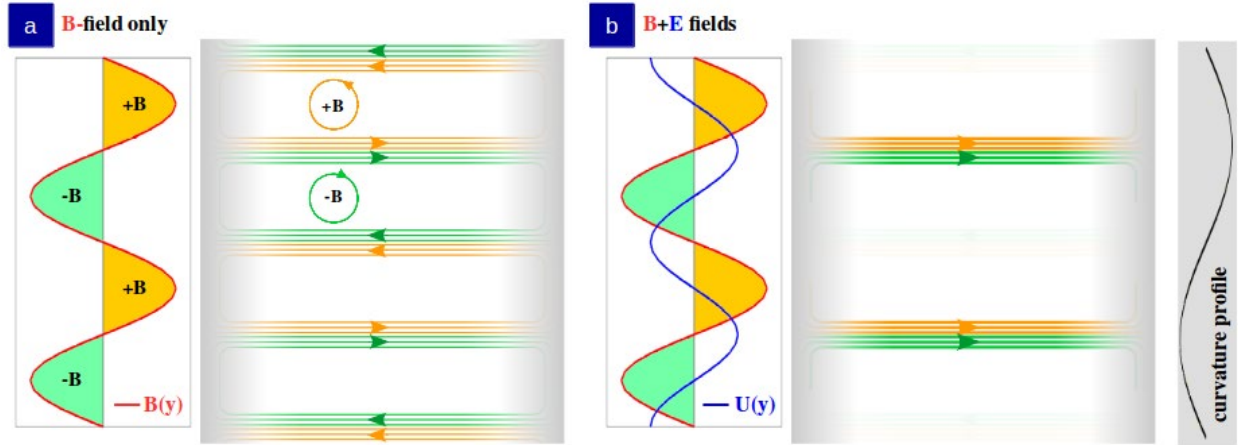


**Figure S5:** Schematics illustrating the effects of spatially oscillating pseudo- (E, B) fields.

### S5: Extreme strain measurement

We estimate strain in our system by comparing Fourier transforms of atomic resolution images taken on unstrained and strained regions (Fig. S6 a, b respectively). As expected, the

unstrained graphene lattice is characterized by hexagonal periodicity with Fourier space peaks (marked by white dashed circles) equidistant from the center, falling on a centered (grey dotted) circle. On the other hand, graphene imaged on the draped region yields a clearly distorted hexagonal lattice, in addition to some superlattice peaks (marked in blue). The deviation in magnitudes of the wavevectors from that of unstrained graphene is used to estimate the strain. Ratios of lattice constants imply strain magnitudes over 10%. This measurement is also consistent with first principle calculations required to reproduce the observed spectra, as discussed in Supplementary sec. 3. Both regions are imaged with the same tip to reduce potential calibration issues. The two regions are also chosen to be close to each other to prevent any non-linearity in piezo expansion.

Previous studies (69) have reported graphene sheets sticking to the STM tips. Such effects are particularly large for micron sized graphene sheets which are free to bend and should not be important for graphene ripples measuring only tens of nanometers and stretched taut under tension. Similar topographic images were obtained with forward and backward motion of the STM tip, proving that the graphene position is not appreciably disturbed by the tip. The forward and backward scans also yielded topographies showing similar strain magnitudes. Increasing the tunneling current by an order of magnitude ( $\sim 100$  pA to  $\sim 1$  nA) did not change the topography, further proving that tip artifacts are negligible in the topography.

We also note that in making measurements from topographies of the draped region, the typical approach to STM analysis of using plane subtraction will, in such a highly sloped region, leads to artificial compression along the draping direction (it is equivalent to projection into a plane parallel to the terraces). Thus we instead rotate the coordinate system in order to properly extract all distances in the draped graphene.

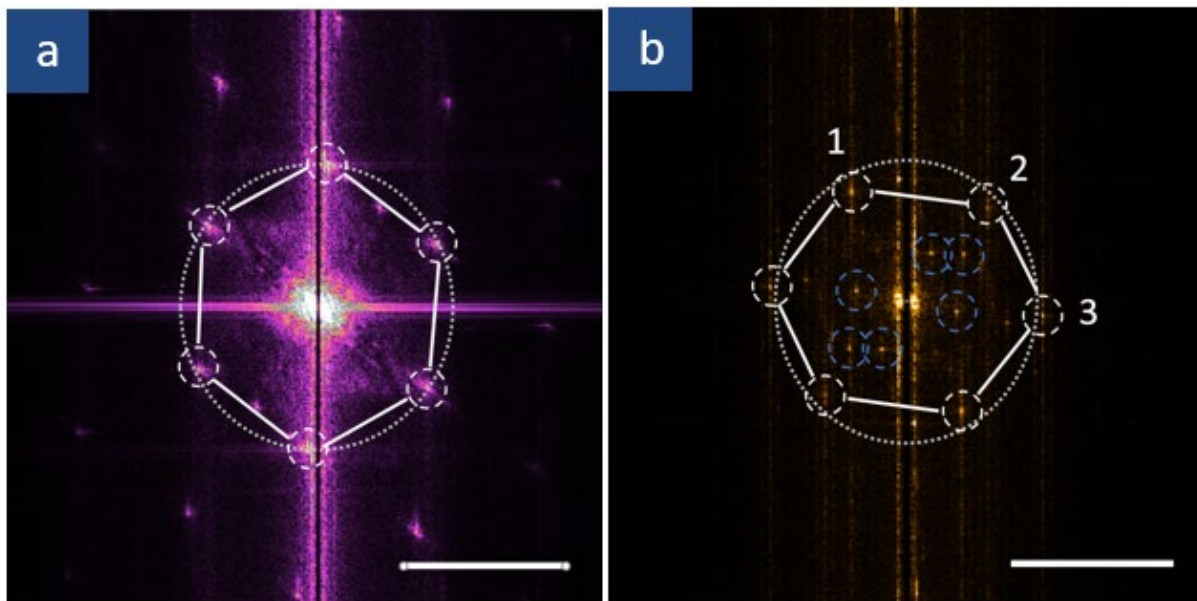


**Figure S6:** Direct measurement of extreme strain: (a) FFT of atomic resolution topography from an unstrained graphene lattice. Peaks (marked by white dashed circles for clarity) are equidistant from the center (as grey dotted circle). (b) Topographic FFT from the draped region shows superlattice components (blue circles) and lattice distortion due to strain. Measuring deviation from the unstrained positions (grey circle) yields strains of 1) 10.3%, 2) 6.8% and 3) -3.3%. Scalebars in both figures are  $5 \text{ nm}^{-1}$ . ( $=1/2 \text{ Å}$ )

### S6: $E_n \propto n$ plots

In Fig. 2c we plotted the background subtracted spectra taken on STREMS and plotted the energy dependence of the peaks for Spectrum #19 in Fig. 2d. In Fig. S7, we show the linear fits for all the twelve spectra taken on the draped part (numbered #8-19) with their linear fits. We observe that the higher energy peaks deviate more from the linear fits. This can be attributed to the fact that graphene dispersion deviates from being linear at higher energies away from the Dirac point.

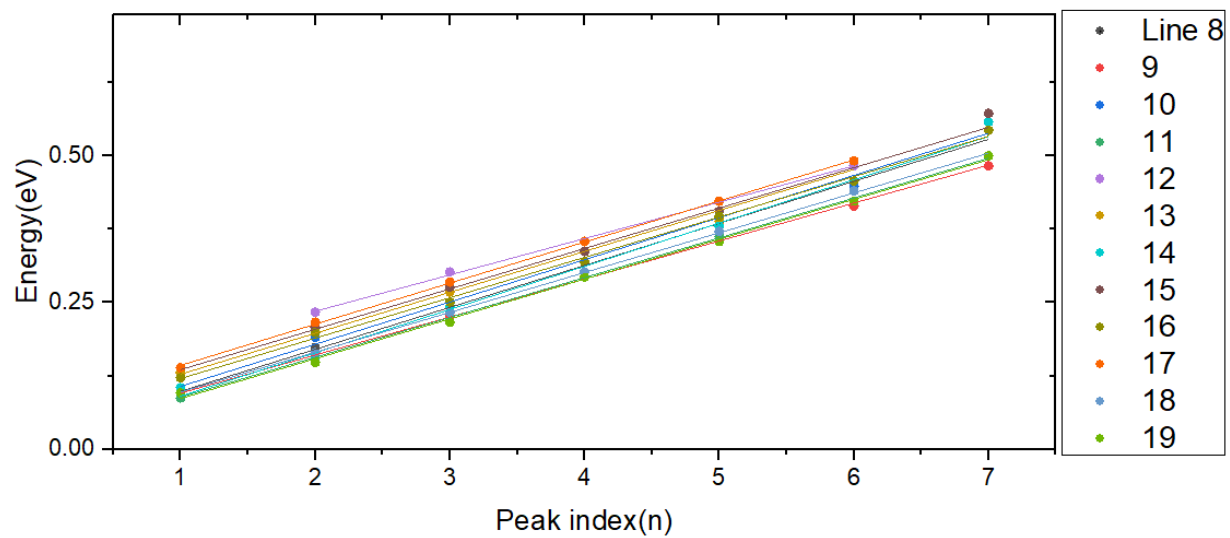


**Figure 7:** All twelve background subtracted spectra (Line #8-19) taken on the STREMS and shown in Fig. 2c of the text have equally spaced peaks.